

Anomalous temperature-dependent magnetization in the nearly collinear antiferromagnet Y_2Co_3

Yunshu Shi,¹ Huibo Cao,² Hung-Cheng Wu,^{3,4} Li Yin,⁵ Neil Harrison,⁶ David S. Parker,⁵ Tushar Bhowmick,⁷ Tessa McNamee,⁷ Fatemeh Safari,^{7,8} Sergey L. Bud'ko,^{9,10} James C. Fettinger,¹¹ Susan M. Kauzlarich,¹¹ Peter Klavins,¹ Dmitry Popov,¹² Ravhi Kumar,⁸ Russell J. Hemley,^{8,13} Shanti Deemyad,⁷ Taku J. Sato,³ Paul. C. Canfield,^{9,10} and Valentin Taufour^{1,*}

¹*Department of Physics and Astronomy, University of California, Davis, California 95616, USA*

²*Neutron Scattering Division, Oak Ridge National Laboratory, Oak Ridge, Tennessee 37831, USA*

³*Institute of Multidisciplinary Research for Advanced Materials, Tohoku University, Sendai 980-8577, Japan*

⁴*Department of Physics, National Sun Yat-sen University, Kaohsiung, 80424, Taiwan*

⁵*Materials Science and Technology Division, Oak Ridge National Laboratory, Oak Ridge, Tennessee 37831, USA*

⁶*Los Alamos National Laboratory, Los Alamos, New Mexico 87545, USA*

⁷*Department of Physics and Astronomy, University of Utah, Salt Lake City, Utah 84112, USA*

⁸*Department of Physics, University of Illinois Chicago, Chicago, Illinois 60607, USA*

⁹*Department of Physics and Astronomy, Iowa State University, Ames, Iowa 50011, USA*

¹⁰*Ames National Laboratory, US DOE, Iowa State University, Ames, Iowa 50011, USA*

¹¹*Department of Chemistry, University of California, Davis, California 95616, USA*

¹²*HPCAT, X-ray Science Division, Argonne National Laboratory, Lemont, Illinois 60439, USA*

¹³*Department of Chemistry, University of Illinois Chicago, Chicago, Illinois 60607, USA*

Y_2Co_3 is a newly discovered antiferromagnetic (AFM) compound with distorted kagome layers. Previous investigations via bulk magnetization measurements suggested a complex noncollinear magnetic behavior, with magnetic moments primarily anti-aligned along the b axis and some canting towards the ac plane. In this study, we report the magnetic structure of Y_2Co_3 to be an A-type AFM structure with ferromagnetic (FM) interactions within the distorted kagome plane and an interplane antiferromagnetic interaction, as determined by single-crystal neutron diffraction. The magnetic moments align along the b axis, with minimal canting towards the c axis, at odds with the previous interpretation of bulk magnetization measurements. The magnetic moments on the two distinct Co sites are $[0, -0.68(3), 0] \mu_B$ and $[0, 1.25(4), 0.07(1)] \mu_B$. We attribute the previously reported “noncollinear” behavior to the considerable temperature dependence of itinerant AFM exchange interactions, induced by thermal contraction along the b axis. Additionally, our examination of lattice constants through pressure studies reveals compensating effects on FM and AFM interactions, resulting in negligible pressure dependence of T_N .

I. INTRODUCTION

Antiferromagnetism in kagome lattices has attracted significant interest within the condensed matter community because of the potential emergence of exotic quantum states from the unique lattice structure and frustrated magnetic ordering at low temperatures. Novel magnetic and transport properties may arise from these phenomena, such as quantum spin liquid states¹, flat bands², and the anomalous Hall effect^{3,4}. The $\text{R}_2\text{Co}_{3-x}\text{Si}_x$ ($\text{R} = \text{Y}, \text{La}, \text{Ce}, \text{Pr}, \text{Nd}, \text{and Gd}; 0 \leq x < 0.5$) family, featuring the La_2Ni_3 -type structure, hosts distorted kagome lattices within the ac plane. Most compounds in this family are ferromagnetic (FM)^{5,6} or ferrimagnetic⁷, with magnetic moments originating from both rare-earth elements and cobalt.

Y_2Co_3 and La_2Co_3 are among the richest Co-based antiferromagnets, exhibiting relatively high Néel temperatures of 252 K and 315 K^{8,9}, respectively. Prior research on single-crystal Y_2Co_3 ⁸ revealed antiferromagnetic ordering with magnetic moments primarily aligned along the b axis. Bulk magnetization measurements exhibited temperature-dependent susceptibility along the hard axes and a relatively large nonzero susceptibility along the easy axis at low temperatures. This behavior was interpreted as a complex noncollinear magnetic structure. In contrast, we report single-crystal neutron diffraction measurements, which indicate an almost collinear A-type antiferromagnetic structure.

The observed discrepancy is carefully examined in this paper. The temperature dependence of perpendicular magnetic susceptibility is explained by the relatively large temperature dependence of the AFM interaction owing to the thermal contraction below the transition temperature. By comparing the Grüneisen parameter of Y_2Co_3 with other Y-Co compounds¹⁰, we demonstrate that the change in lattice constants across the wide temperature range may increase the AFM exchange interaction by up to 40%, consequently decreasing the perpendicular magnetic susceptibility by 30%, resembling that of a noncollinear antiferromagnet. We further reveal that the intraplane ferromagnetic interaction and interplane antiferromagnetic interaction have compensating dependencies on lattice parameters. This finding may also account for the previously reported small pressure dependence of T_N and the “robustness” of antiferromagnetism in this compound. Nevertheless, the presence of nonzero parallel magnetic susceptibility remains puzzling. We rule out sample misalignment and minimal canting moment along the c axis as possible explanations. We hypothesize that residual easy axis magnetic susceptibility may originate from the itinerant antiferromagnetic fluctuations, as supported by both experimental evidence and spin-polarized density function theory (DFT) calculations.

II. METHODS

Single crystals of Y_2Co_3 were synthesized using the flux growth method⁸. A starting composition of $Y_{51.5}Co_{48.5}$ was arc-melted and sealed in a clean tantalum crucible with a tantalum filter¹¹. The tantalum assembly was sealed in a silica tube with partial argon pressure. The sample was then heated up to 1150 °C within 4 hours and held for 5 hours, quickly cooled down to 945 °C and slowly cooled down to 825 °C within 133 hours.

Neutron single-crystal diffraction was performed to determine the magnetic structure at the DEMAND instrument (HB-3A beamline) in its four-circle mode at the High Flux Isotope Reactor of the Oak Ridge National Laboratory¹². A neutron wavelength of 1.542 Å was used from a bent perfect Si-220 monochromator¹³. The magnetic and nuclear peaks are collected at 5 K. The Bilbao Crystallography Server was used for the magnetic symmetry analysis¹⁴. Magnetic structure refinements were carried out with the FullProf Suite program¹⁵.

To determine the weak magnetic component along the c axis, single-crystal neutron diffraction measurements were also performed using the GPTAS (4G) triple-axis thermal neutron spectrometer in two-axis mode (without an analyzer) at JRR-3, Tokai, Japan¹⁶. The incident neutron was selected at 14.7 meV using a vertically focusing PG 002 monochromator. To eliminate higher harmonic neutron contributions, two PG filters were inserted, one after the monochromator and another after the sample. A single crystal of Y_2Co_3 , weighing approximately 30 mg, was aligned in the $(h0l)$ plane as scattering planes. The crystal was sealed in a standard aluminum sample can with 4He exchange gas. Cooling was achieved using a Gifford-McMahon (GM) cryostat equipped with a closed-cycle 4He refrigerator. $\theta-2\theta$ scans were performed to obtain the $|F|^2$ table, after correcting for the Lorentz-polarization factor.

Magnetization measurements were performed with a Magnetic Property Measurement System (MPMS, Quantum Design) in the temperature range 2 K–300 K with the applied magnetic fields up to 7 T. The angle-dependent magnetization measurements at constant temperatures 2, 5, and 10 K and applied field 20 kOe were performed using a horizontal rotator option of a Quantum Design MPMS3 SQUID magnetometer. The sample was aligned with the rotation axis visually, using characteristic features of its morphology and glued to the rotator platform with a small amount of GE-7031 varnish. The direction of the magnetic field was changing in the ab and ac crystallographic planes. Empty rotator measurements were performed at the same H, T conditions as well, but since the angular change of the empty rotator response was three orders of magnitude smaller than that of the sample, no background subtraction was performed.

Resistivity, Hall resistivity, and heat capacity measurements were carried out with a Physical Property Measurement System (PPMS, Quantum Design). Resistivity data was measured using the four-probe method with the current in the ac plane. The Hall resistivity measurement was applied using the five-probe method. The magnetic field was swept from 9 T to -9 T to remove the longitudinal signal, which is an even

function of the field.

III. RESULT AND DISCUSSION

A. Magnetic structure

Figure 1(a) exhibits the selected magnetic $(01\bar{1})$ Bragg reflection as a function of temperature from 5 K to 300 K. Below the Néel temperature ($T_N \sim 252$ K) a pure magnetic signal develops at the $(01\bar{1})$ Bragg position indicating that the magnetic moments have a component along a direction perpendicular to $(01\bar{1})$. This result is compatible with the moments along the b axis. A transition temperature of around 250 K is consistent with that obtained from single-crystal magnetization measurement.

The magnetic symmetry analysis using Bilbao Crystallography Server with the magnetic propagation vector of $\vec{k} = (010)$ and Wyckoff positions of two Co sites being 4b and 8e, yields eight possible magnetic space group candidates. The magnetic space group P_{Accn} (BNS notation: No. 56.374) is the only model that satisfies the observed magnetic reflections in the refinement, as shown in Fig. 1(b). The resolved magnetic structure is displayed in Fig. 2(a), where the Co (8e) site has a magnetic component only along the b axis [$\mathbf{m}_{8e} = (0, -0.68(3), 0) \mu_B$] and the Co (4b) site has a major magnetic moment along the b axis and a minor component along the c axis [$\mathbf{m}_{4b} = (0, 1.25(4), 0.03(8)) \mu_B$]. However, the refine c component is too small to be determined within the instrument's resolution.

The overall magnetic moments appear relatively small compared to the local moment of Co ($1.7 \mu_B/Co$) or the effective moment of $\mu_{eff} = 2.513(4) \mu_B/Co$ ⁸ obtained from the Curie-Weiss fitting above the transition temperature, suggesting some degree of itinerant character in Y_2Co_3 . Within each layer of the ac plane, Co moments order ferromagnetically, while the antiferromagnetic alignment is along the b axis between layers of Co atoms separated by Y atoms. The intraplane ferromagnetic interactions discovered in the neutron diffraction experiment coincide with the positive Curie-Weiss temperature obtained by Curie-Weiss fitting⁸, which will be discussed in details later.

Simulations of magnetic structure factors indicate that the magnetic moment along the c axis at the Co (4b) site results in specific magnetic reflection peaks along $(h00)$, following the extinction rule $h = 2n + 1$. To further confirm the weak tilting moment along the c axis, the sample was aligned to the $(h0l)$ plane as a scattering plane. As shown in Fig. 3, at room temperature, there is no observable reflection at (100) reflection, consistent with the space group of $Cmce$ (No. 64). At 3.8 K, the magnetic (100) reflection is clearly observed, indicating the formation of a magnetic moment along the c axis. A scale factor was determined from the (200) nuclear reflection. The calculated moment size based on (200) nuclear reflection and (100) magnetic reflection at 3.8 K was $0.07(1) \mu_B$, which provides a more precise determination than the previously mentioned value of $0.03(8) \mu_B$ from magnetic structure refinement.

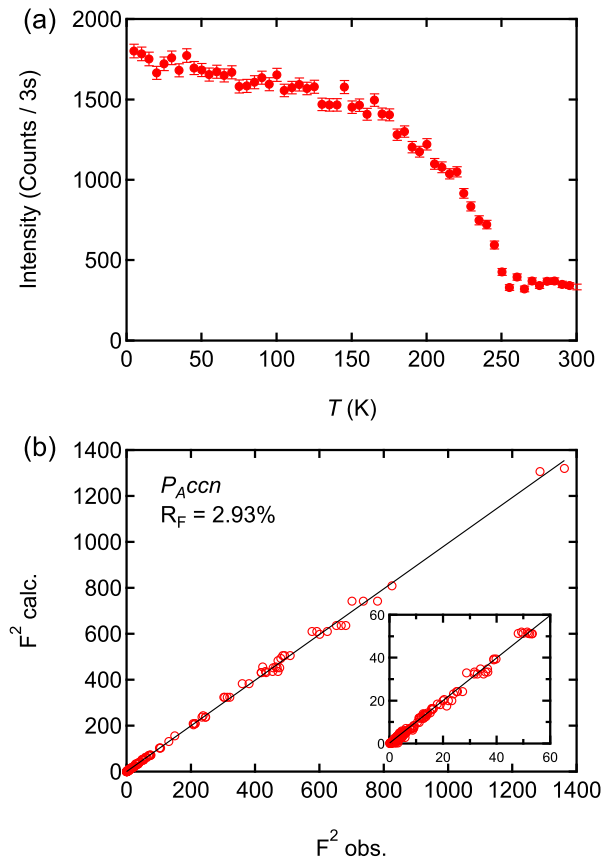


FIG. 1. (a) The $(01\bar{1})$ magnetic Bragg peak intensity as a function of temperature, corresponding to the squared magnetic order parameter. (b) The calculated magnetic structure factor ($|F|^2_{calc.}$) derived from the refinement, assuming the magnetic space group of P_{Accn} , compared to the observed magnetic structure factor ($|F|^2_{obs.}$) obtained at 1.5 K. The inset illustrates the distribution on the lower side of $|F|^2$. The linear relation between $|F|^2_{calc.}$ and $|F|^2_{obs.}$ indicates a reliable refinement.

During the extended scan at selected nuclear reflection and magnetic reflection using the 4G instrument, it is noteworthy that we detected measurable intensity at the (201) and (203) reflections at room temperature (in the paramagnetic phase). The occurrence of these reflections is unusual as they are not allowed by the $Cmce$ space group. This suggests that their origin could stem from extrinsic factors, such as higher-harmonic neutrons or double reflections, or possibly from intrinsic symmetry lowering because of the large crystal size. Despite this, the intensity ratio between the strongest (200) reflection and weak (201) reflection is only approximately 0.05%. Consequently, the presence of the (201) reflection is unlikely to significantly affect the analysis of the magnetic structure in this paper.

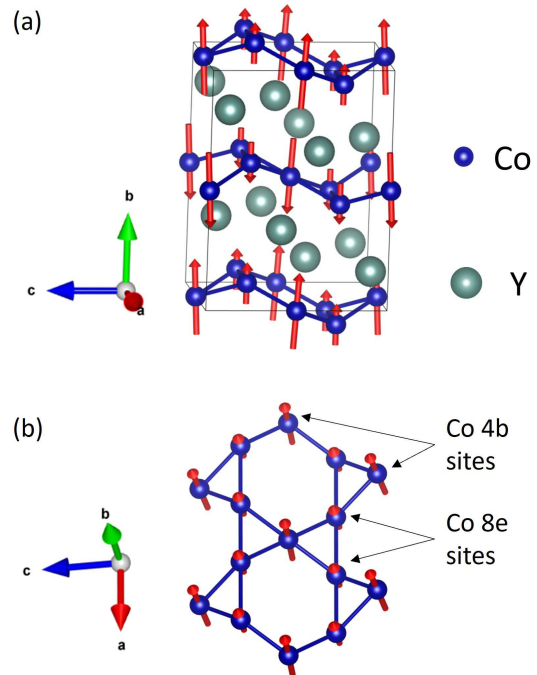


FIG. 2. (a) Illustration of the magnetic Structure of Y_2Co_3 . (b) The magnetic structure of Y_2Co_3 in one Co layer.

B. Temperature-dependent bulk magnetization

The single-crystal neutron diffraction confirms the major magnetic moments along the b axis and reveals an almost collinear magnetic structure. In a collinear Heisenberg antiferromagnet with local moments, the magnetic susceptibility is anticipated to be nearly zero at 0 K along the ordering axis. When the applied field is perpendicular to the ordering axis, the magnetic susceptibility is expected to be temperature independent¹⁷. Examples supporting this theoretical model include Ni_3TeO_6 , $GdNiGe_3$ and MnF_2 ¹⁷⁻¹⁹. However, the bulk magnetization measurements on Y_2Co_3 show a relatively large nonzero susceptibility at 2 K along the ordering b axis. Moreover, when the magnetic field is applied perpendicular to the ordering axis, the susceptibility of Y_2Co_3 decreases as the temperature drops [Fig. 4(a)].

If this bulk susceptibility is attributed to canting, we first try to roughly estimate the canting angle α using χ_b at $T = 2$ K. By decomposing the applied magnetic field into the directions parallel and perpendicular to the magnetic moment, and summing the corresponding susceptibility, we get the formula $\sin^2 \alpha = \frac{\chi_b(0)}{\chi_b(T_N)}$ (see Appendix C). This yields $\alpha = 23^\circ$, a value significantly larger than the observed canting angle of the magnetic moments on the Co (4b) sites, which is approximately 3° as determined by neutron diffraction. Moreover, the temperature dependence in χ_a and χ_c cannot be attributed

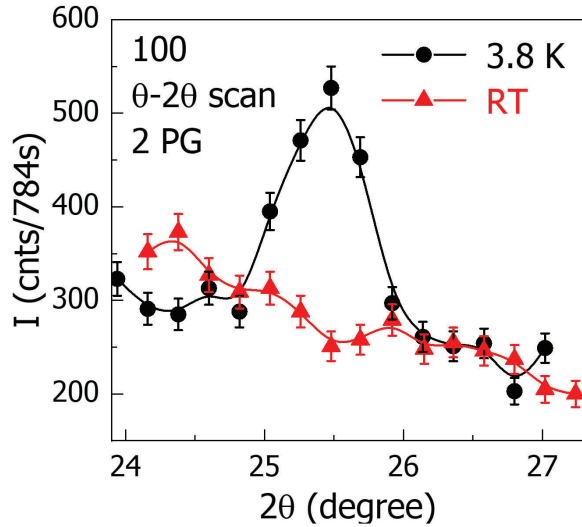


FIG. 3. $\theta-2\theta$ scans performed at 3.8 K and room temperature were used to obtain the integrated intensity of selected 100 reflection, indicating the presence of a magnetic component along the c axis. The magnetic moment of Co (4b) along the c axis was calculated to be $0.07(1) \mu_B$. It is worth noting that magnetic moment along the b axis does not contribute to any magnetic reflection at 100 reflection. The configuration of GPTAS (4G) instrument was set to 40° -PG- 40° - 40° -PG-open, in two-axis mode.

to the c component of the magnetic moment, as magnetization along the a and c axes exhibits identical behavior.

We then check whether a misalignment would be a possible explanation utilizing angular-dependent magnetization measurement. Figures 4(b) and 4(c) show the magnetization as a function of the tilted angle from the b axis toward the a and c axes. The experiment data aligns well with a $\sin^2 \gamma$ function (solid line), where γ is the angle from the b axis. This indicates that the magnetization reaches its minimum exclusively along the b axis, as opposed to other directions. This outcome further confirms that the temperature dependence of the susceptibility cannot be attributed to sample misalignment, which refers to the possibility that the sample might not be perfectly aligned along the intended crystallographic axis during the measurement. Such a misalignment would mean that our measurements could contain contributions from multiple crystallographic directions.

C. The effect of lattice contraction on exchange interaction

Trying to understand the temperature dependence of anisotropic magnetic susceptibility, we use the molecular field theory (MFT) to analyze the two different types of exchange interactions and the previously reported magnetization behavior in more details. In Y_2Co_3 , the interplane antiferromagnetic (AFM) exchange energy J_b and the intraplane ferromagnetic (FM) exchange energy J_{ac} can be estimated from T_N and the Curie-Weiss temperature following MFT. In this frame-

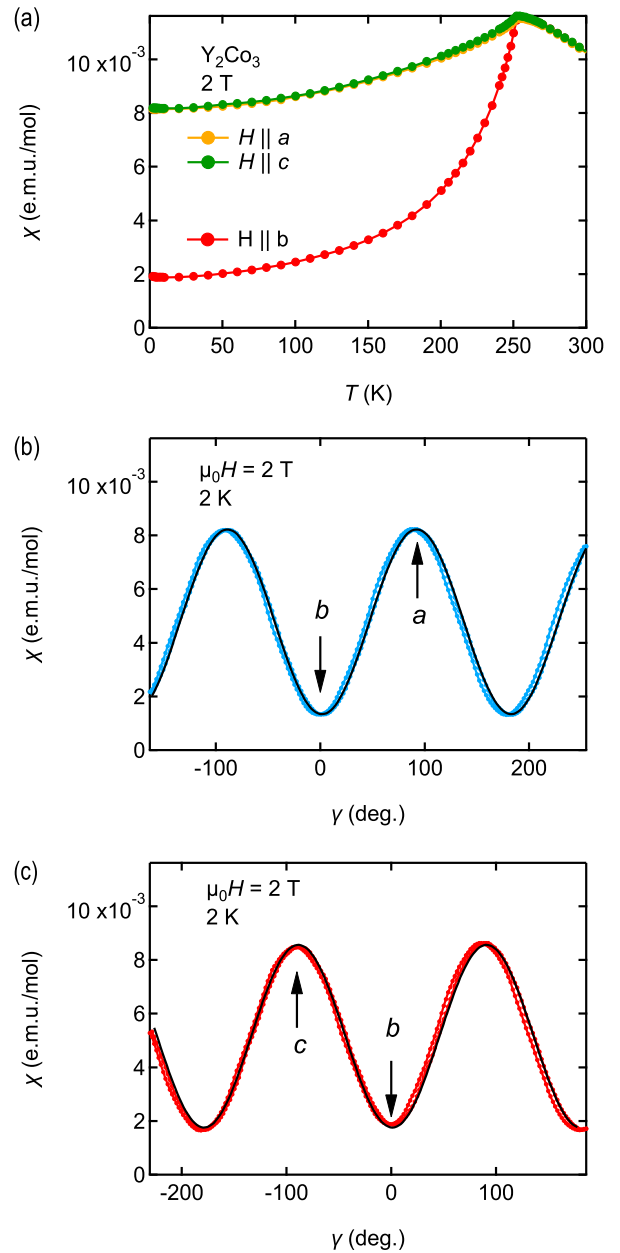


FIG. 4. (a) Susceptibility as a function of temperature of single crystal Y_2Co_3 with the magnetic field along the a , b , and c axes. [(b), (c)] The magnetic susceptibility as a function of γ , where γ is the angle between the magnetic field and the b axis in the $b-a$ plane and $b-c$ plane.

work, a positive exchange energy value indicates FM interactions, while a negative value corresponds to AFM interactions. According to MFT, for a lattice with identical spins, the Curie Weiss temperature θ_P and Néel temperature T_N can be expressed as follows^{17,20,21}:

$$\theta_P = \frac{S(S+1)}{3k_B} \sum_j J_{ij} \quad (1a)$$

$$= \frac{S(S+1)}{3k_B} (z_{ac}J_{ac} + z_bJ_b) \quad (1b)$$

$$T_N = \frac{S(S+1)}{3k_B} \sum_j J_{ij} \cos \phi_{ij} \quad (1c)$$

$$= \frac{S(S+1)}{3k_B} (z_{ac}J_{ac} - z_bJ_b) \quad (1d)$$

In these equations, the sums are taken over the nearest neighbors j around the i th spin, where J_{ij} represents the exchange coupling between the i th and j th spins. Consequently, the summation can be simplified as the product of the exchange coupling and the number of nearest neighbors, with z_{ac} denoting the number of nearest neighbors within the ac plane exhibiting FM exchange couplings, and z_b representing the number of interplane nearest neighbors along the b axis with AFM exchange couplings.

In the case of Y_2Co_3 , the two different cobalt sites are not crystallographically equivalent, nevertheless, the average molecular fields can still be estimated. For an antiferromagnetic compound, there exist molecular field couplings between two different sublattices (λ_d) and within the same sublattice (λ_s). In Y_2Co_3 , λ_d represents the interplane AFM coupling and λ_s represents the intraplane FM coupling. The expressions of these two terms are as follows^{20,22}:

$$\lambda_d = \frac{2z_bJ_b}{Ng^2\mu_B^2} \quad (2a)$$

$$\lambda_s = \frac{2z_{ac}J_{ac}}{Ng^2\mu_B^2} \quad (2b)$$

Thus, Eqs. (1b) and (1d) can be rewritten as

$$\theta_P = \frac{Ng^2\mu_B^2S(S+1)}{6k_B} (\lambda_s + \lambda_d) = \frac{C}{2} (\lambda_s + \lambda_d) \quad (3a)$$

$$T_N = \frac{Ng^2\mu_B^2S(S+1)}{6k_B} (\lambda_s - \lambda_d) = \frac{C}{2} (\lambda_s - \lambda_d) \quad (3b)$$

where N is number of spins and $C = \frac{Ng^2\mu_B^2S(S+1)}{3k_B}$ is the Curie constant. With $T_N = 252$ K and $\theta_P = 59.5$ K, the intra- and interplane molecular fields can be estimated to be $C\lambda_s \approx 312$ K and $C\lambda_d \approx -192$ K.

Along the perpendicular direction, the magnetic susceptibility can be expressed as (see Appendix B)

$$\chi_{\perp}(T) = \frac{2M^2(T)}{2|\lambda_d|M^2(T) + K(T)} \quad (4)$$

In this equation, $M(T)$ is the spontaneous magnetization of the sublattices, and $K(T)$ is the temperature-dependent magnetocrystalline anisotropy. At 2 K, $K = 5.74$ J/mol Co⁸ is

much smaller than the exchange term $|\lambda_d|M^2 \approx 200$ J/mol Co using the value of $C\lambda_d = -192$ K, the Curie constant obtained from the Curie-Weiss fitting⁸ and $M = \frac{1}{2}N_A g \mu_B S$. Consequently, the temperature dependence of the $K(T)$ term (see Appendix D) would only cause a change in χ_{\perp} of less than 3%, indicating that the large drop of perpendicular magnetic susceptibility can not be explained by magnetocrystalline anisotropy. Equation (4) can be simplified as

$$\chi_{\perp}(T) = \frac{1}{|\lambda_d|} \quad (5)$$

We propose that the decrease in the perpendicular magnetic susceptibility is attributed to the enhancement of the AFM exchange interaction. This hypothesis is preliminarily evaluated by comparing the exchange coupling constants at high and low temperatures. As previously noted, the $C\lambda_d$ value near the transition temperature is -192 K, while at 2 K, this value is estimated to be approximately -303 K, based on the previously reported spin-flop field and the magnetocrystalline anisotropy energy⁸. A more detailed discussion of this estimation is presented in Appendix D. The smaller absolute value of λ_d at higher temperature indicates that the exchange coupling strength increases as the temperature decreases. We propose that this is caused by thermal contraction along the b axis upon cooling. Figure 5 shows the change of lattice parameters a , b , and c as a function of temperature obtained from single-crystal neutron diffraction. Because of limited beam time, measurements were confined to a and c parameters during the cooling and warming procedures, with the behavior of b deduced through interpolation based on the two data points at 90 K and 290 K and the temperature dependence of a . We observe that the thermal contraction exhibits a distinct change in slope at the AFM transition temperature, indicating strong coupling between the AFM ordering and lattice parameters. This suggests that thermal contraction upon cooling could enhance the antiferromagnetic coupling, resulting in the observed temperature dependence of χ_{\perp} . This explanation can apply more generally to other materials. For example, other Co-based antiferromagnetic materials with collinear magnetic structures, such as $KCoF_3$, K_2CoF_4 , and $Co_2Mo_3O_8$, also show a slight decrease in perpendicular magnetic susceptibility upon cooling²³⁻²⁶. Notably, upon cooling, there is an expansion along the a axis leading to an increased distortion of the kagome lattice in the ac plane.

To explore the relationship between the AFM exchange interaction and the lattice parameter b , we calculate the volume Grüneisen parameter, $\Gamma^i = -d \ln |J| / d \ln a_i$ ^{10,27} of the AFM component, where J is the exchange energy, and a_i represents the lattice constant of the orthorhombic axes and/or the volume. Referring to Eqs. (2a) and (5), we derive $\Gamma^b = d \ln \chi_{\perp} / d \ln b \approx 66$ (see Fig. 6). The positive sign indicates that the AFM coupling becomes stronger as the temperature decreases, which is also seen in other Co-based antiferromagnetic compounds, such as K_2CoF_4 and $RbCoF_3$. However, the magnitude value of Γ^i in Y_2Co_3 is much larger than those of K_2CoF_4 and $RbCoF_3$, where Γ^i is around 15²⁸. This larger value is rationalized by the larger interlayer Co-Co distance

in Y_2Co_3 (4.75 Å) compared to the distance between Co^{2+} cations in K_2CoF_4 and RbCoF_3 (\sim Å). These materials have lower T_N values and smaller Grüneisen parameters. Consequently, the effect of thermal contraction on their exchange interactions is less pronounced than in Y_2Co_3 . We note that the temperature dependence of χ_\perp in K_2CoF_4 has been explained previously using the perturbation of the Ising model²⁹, but the proposed 2D Ising model is not applicable to Y_2Co_3 . It is possible that the lattice contraction effects also play a role in K_2CoF_4 .

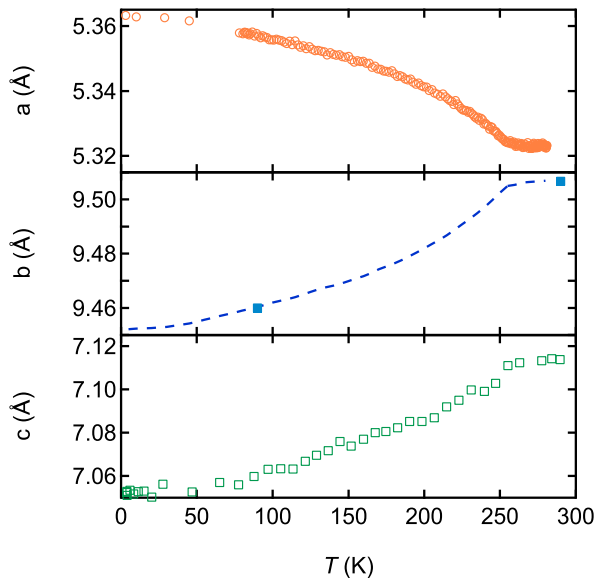


FIG. 5. The lattice parameter as a function of a , b , and c . The markers are experimental data, and the dashed line is the interpolated curve. Because of limited beam time, measurements were confined to a and c parameters during the cooling and warming procedures, with the behavior of b deduced through interpolation based on the two data points at 90 K and 290 K, and the temperature dependence of a .

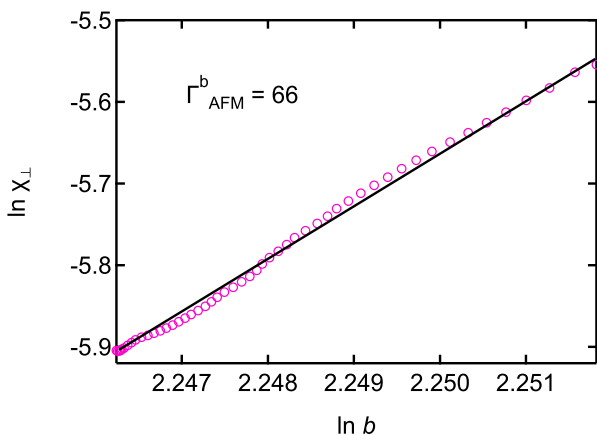


FIG. 6. $\ln \chi_\perp$ as a function of $\ln b$ below T_N showing linear relationship.

The itinerant nature of Y_2Co_3 cannot be fully described by the localized superexchange model. Thus, the impact of lattice contraction on the exchange coupling in Y_2Co_3 is further compared to other Y-Co compounds with itinerant behavior. In the Y-Co system, pressure studies have systematically investigated the correlation between Curie temperature T_C and lattice constants¹⁰. Table I shows the pressure dependencies of T_C , the values of $\Gamma^V = -\frac{d \ln T_C}{d \ln V}$, and the compressibilities (κ) of various Y-Co compounds, revealing a clear trend: a lower Co content correlates with higher compressibility, reduced T_C , a greater sensitivity of T_C to pressure ($\frac{dT_C}{dp}$), and thus a larger Γ^V . Among these compounds, YCo_3 has the highest Γ^V value of -15.1 . Taking the relationship that $d \ln V = \sum_i d \ln a_i$, the Grüneisen parameter along each axis Γ^i is approximately three times that of Γ^V , resulting in $\Gamma^i \approx -45$ for YCo_3 . This value is comparable to that of Y_2Co_3 , despite the different signs owing to the different types of exchange involved.

Notably, the pressure dependence of T_N ($\frac{dT_N}{dp} = -1.65 \text{ K/GPa}$)⁸ in Y_2Co_3 is markedly lower compared to $\frac{dT_C}{dp}$ in other Y-Co compounds, despite similar compressibilities observed in our pressure studies of Y_2Co_3 (see Appendix A). This is because $T_N = \frac{C}{2}(\lambda_s - \lambda_d)$ is determined by both the intraplane FM and interplane AFM interactions. Lattice contraction under pressure suppresses ferromagnetic exchange within the kagome plane, which is consistent across other Y-Co compounds while enhancing antiferromagnetic exchange caused by reduced interplane separations. Thus, the pressure dependence of these two components needs to be analyzed separately. The influence of pressure on the AFM exchange in Y_2Co_3 is quantitatively assessed through Γ^b using the equation $\frac{1}{C\lambda_d} \frac{d(C\lambda_d)}{dp} = \kappa_b \Gamma_{\text{AFM}}^b$, where κ_b denotes the compressibility along the b axis. This yields $\frac{d(C\lambda_d/2)}{dp} = -23 \text{ K/GPa}$. The FM interaction dependence on pressure can then be calculated by $\frac{d(C\lambda_s/2)}{dp} = \frac{dT_N}{dp} + \frac{d(C\lambda_d/2)}{dp} = -24.65 \text{ K/GPa}$, comparable to that of other Y-Co compounds with itinerant ferromagnetic ordering. Consequently, T_N exhibits minimal variance under pressure as a result of compensating FM and AFM interactions. The Grüneisen parameter of the FM exchange interaction within the ac plane, denoted as Γ_{FM}^{ac} , can be similarly calculated using the equation $\frac{1}{C\lambda_s} \frac{d(C\lambda_s)}{dp} = \kappa_{ac} \Gamma_{\text{FM}}^{ac}$, yielding a value of approximately -23 .

D. The evidence for itinerant behavior from physical property measurements

The decrease of the perpendicular magnetic susceptibility is well explained by the increase of the AFM exchange interaction at lower temperatures. However, the origin of the nonzero parallel magnetic susceptibility remains an open question. The magnetic structure of this compound is complicated because of the existence of competing ferromagnetic and antiferromagnetic interactions of the $3d$ electrons in the regime between local and itinerant characters. It has been seen in

TABLE I. The transition temperature T_C or T_N , compressibility κ , pressure dependence of transition temperature $\frac{dT_C}{dp}$, and the Grüneisen parameter Γ^i of Y-Co compounds.

Compound	Type	T_C or T_N (K)	κ (10^{-3} GPa $^{-1}$)	$\frac{dT_C}{dp}$ (K GPa $^{-1}$)	Γ_{FM}^V	Ref			
Y ₂ Co ₁₇	FM	1167	6.7	-3	-0.4	10			
YCo ₅	FM	977	7.5	-10	-1.6	10			
Y ₂ Co ₇	FM	639		-33	-6.4	10			
YCo ₃	FM	301	8.5	-38	-15.1	10			
YCo ₂	PM		9.8			10			
Y ₂ Co ₃	AFM	252	12.4	$\frac{dT_N}{dp}$	$\frac{d(C\lambda_s/2)}{dp}$	$\frac{d(C\lambda_d/2)}{dp}$	Γ_{FM}^{ac}	Γ_{AFM}^b	This paper
				-1.65	-24.65	-23	-23	66	

TiAu, an itinerant antiferromagnetic compound without magnetic constituents, that the magnetic susceptibility shows typical AFM behavior with a value of 10^{-3} e.m.u./mol at the low temperature while displaying the Curie-Weiss behavior above the transition temperature³⁰. The residual magnetic susceptibility at low temperature of TiAu is comparable to that of Y₂Co₃. In this paper, we propose that the itinerant AFM component may contribute to the nonzero magnetic susceptibility seen in Y₂Co₃. Here, we show some evidences of the itinerant AFM component from both Hall measurements and heat capacity results.

Figure 7 displays the transport properties of Y₂Co₃. The comparatively low resistivity signifies good metallic behavior. The derivative (black curve) exhibits a sudden jump at T_N , corresponding to the reduction of scattering from the disordered state to the ordered state. Notably, this compound does not exhibit the typical resistivity increase owing to gap opening associated with spin density waves. However, similar decreases in resistivity have also been observed in other itinerant antiferromagnetic (IAFM) compounds containing d electrons, such as CaCo₂P₂³¹, TiAu³⁰, and BaFe₂As₂³².

Figure 8 shows the magnetic field dependence of the Hall resistivity at various temperatures from 5 K to 300 K. The Hall coefficient shows a strong temperature dependence and undergoes a change in sign at approximately 200 K. The charge density is estimated to be $n_h = 2.75 \times 10^{21}$ cm $^{-3}$ for holes at 5 K and $n_e = 2.52 \times 10^{22}$ cm $^{-3}$ for electrons at 300 K. The temperature-dependent sign reversal of the Hall coefficient clearly indicates multiband contributions and change of the band structure. It is worth noting that this sign reversal occurs in close proximity to T_N , suggesting that the change in the band structure near the Fermi level is likely induced by the magnetic ordering. This observation provides further support for the non-negligible influence of an itinerant antiferromagnetic component.

The presence of the itinerant AFM component is also supported by the small magnetic entropy S_M near the transition. Figure 9(a) shows the specific heat of Y₂Co₃ as a function

of temperature. The lattice specific heat is estimated with the Debye-Einstein model with three acoustic branches and $(3n - 3)$ optical branches, where $n = 10$ is the number of atoms in one primitive cell. The Debye temperature and Einstein temperature are $T_\Theta = 91$ K and $T_E = 225$ K, respectively. A fit with Debye only gave unphysical results reflecting the importance of the optical phonon modes. The specific heat of the magnetic ordering is calculated following the MFT model²⁰ and compared with the experiment data. By subtracting the lattice specific heat, one can obtain the magnetic specific heat across the transition. The magnetic entropy change is estimated to be 1.7 J/(K mol) or 0.56 J/K per Co, which is only 10% of $R \ln 2$.

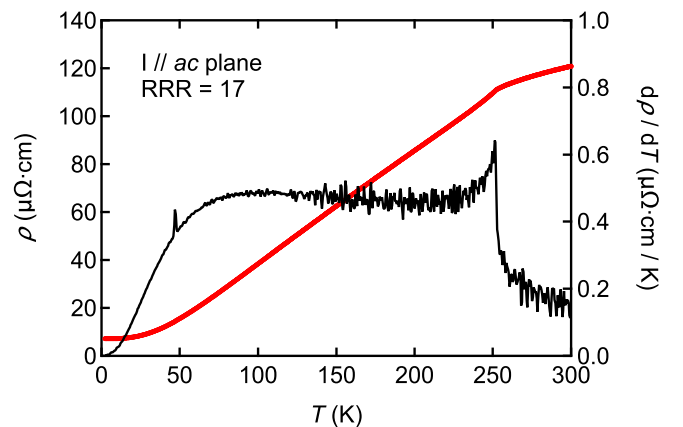


FIG. 7. Resistivity of Y₂Co₃ and its derivative as a function of temperature. A sudden change of slope corresponding to the AFM transition at 252 K is observed.

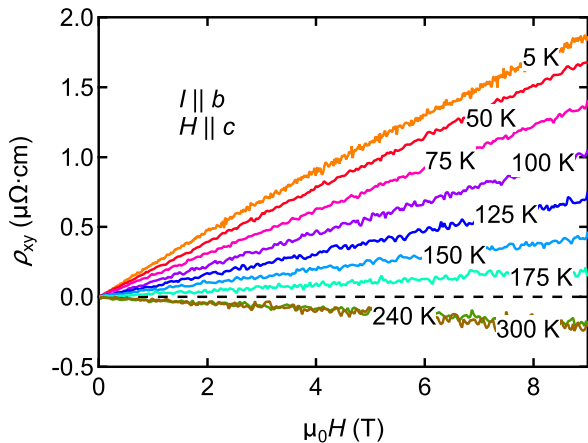


FIG. 8. The Hall resistivity as a function of applied magnetic field along the c axis at various temperatures.

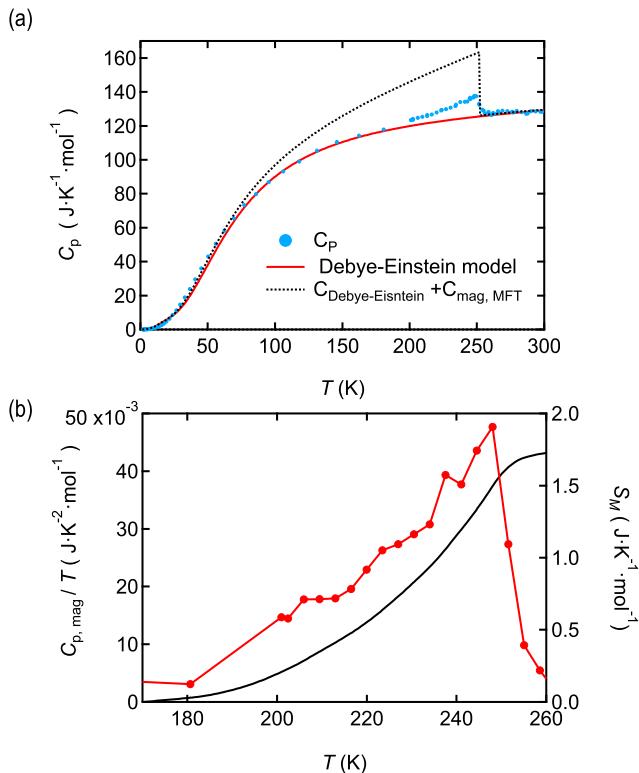


FIG. 9. (a) Specific heat of Y_2Co_3 . The solid-red line is the calculated lattice specific heat using the Debye-Einstein model. The dashed-black line is the total calculated specific heat. The magnetic specific heat is calculated following the MFT model. (b) Magnetic specific heat and magnetic entropy S_M .

IV. SPIN-POLARIZED DFT CALCULATIONS

In order to shed light on the magnetic behavior described in the above experiments we have conducted detailed calculations of the magnetic ground state (moments parallel to the

b axis, successive kagome planes anti-aligned) depicted in Fig. 2(a). Details of these calculations may be found in our previous publication⁸.

In general, the calculations do a rather good job of describing the observed magnetic ground state, at least with respect to the collinear component considered here. We find moments on the $8e$ and $4b$ sites of, respectively, 0.84 and $1.43 \mu_B/Co$, in reasonable agreement with the experimental values of $0.68(3)$ and $1.25(4) \mu_B/Co$. The larger theoretical values may originate in any of a number of factors. These would include the standard first-principles neglect of fluctuations, and our use of the generalized gradient approximation, which for itinerant systems can overstate magnetic order relative to the local density approximation. Nevertheless, we reproduce both the relative moment size ordering of the two distinct Co sites in this complex structure, the general magnitude of these moments, and the energetic favorability of the ground state itself, relative to other states such as a ferromagnetic configuration, which falls some 6 meV/f.u higher in energy.

In addition, our calculations find the b axis as the easy axis, again as found experimentally, with this axis more stable than the a axis by an energy value of 0.15 MJ/m^3 and the corresponding value with respect to the c axis rather larger at 0.90 MJ/m^3 . This is contrary to the experimental result where we find a small canting along c , but not along a . This highlights the limits of DFT calculations for such small energy scales. These two values bracket the experimental value for hcp, ferromagnetic cobalt of approximately 0.7 MJ/m^3 . These values may be regarded as relatively typical for $3d$ -based compounds such as Y_2Co_3 , and rather smaller than those, such as YCo_5 , of the $CaCu_5$ structural type, which display an order of magnitude larger magnetic anisotropy.

These typical anisotropy values in Y_2Co_3 arise despite the presence here of kagome-type planes, although highly distorted, as in the $CaCu_5$ structural type and speak to the importance of both the intervening (between Co layers) yttrium plane, and the particular stoichiometry of Y_2Co_3 in determining the magnetic ground state and its interaction with the lattice.

We also note from Fig. 14(b) (see Appendix D) that the experimentally observed exchange field – that required to fully polarize the material into a ferromagnetic state – is likely well in excess of 100 T . This indicates that the magnetism in this compound is in fact rather robust, as found in our previous publication. We note that this occurs despite the fact that both the calculated and observed magnetic moment values are significantly smaller than those in cobalt itself, indicative of the complexity of the magnetic interactions in Y_2Co_3 .

Finally, note that, as detailed in our previous publication on Y_2Co_3 , there is significant evidence even from the first-principles calculations of the itinerant character described experimentally above. In particular, certain magnetic configurations, when initialized (such as a *ferrimagnetic* state described in that work), spontaneously change in the course of the calculation convergence to a different magnetic configuration, while others – such as one with Co-Co nearest-neighbors anti-aligned – simply fail to converge. Both these results are strong theoretical indications that the magnetism, while clearly con-

taining elements of local character, also possesses a degree of itinerant behavior. This is indeed a complex behavior that could not have reasonably been anticipated, and suggests that even among materials one would expect to be easy to describe, unanticipated surprises may be present.

V. CONCLUSION

In summary, this study presents the magnetic structure of Y_2Co_3 . single-crystal neutron diffraction reveals that Y_2Co_3 forms an almost collinear A-type antiferromagnetic structure, with ferromagnetic interaction within the distorted kagome plane and antiferromagnetic interaction between planes. The magnetic moments on the two distinct Co sites are $[0, -0.68(3), 0] \mu_B$ and $[(0, 1.25(4), 0.07(1))] \mu_B$, respectively. We addressed the discrepancy between the almost collinear magnetic structure and the anomalous temperature dependence of the bulk magnetization within the local and itinerant regimes. We show that the AFM exchange interactions are strongly affected by lattice constants, resulting in a large temperature dependence of the perpendicular magnetic susceptibility. The itinerant AFM component may explain the nonzero parallel magnetic susceptibility at low temperatures, as indicated by resistivity measurements and the minimal entropy change observed in heat capacity measurements. First-principles calculations support these results.

ACKNOWLEDGEMENT

We thank D. C. Johnston for useful discussions. Y.S. and V.T. acknowledge support from the UC Laboratory Fees Research Program (LFR-20-653926) and the UC Davis Physics Liquid Helium Laboratory Fund. Part of this research used resources at the High Flux Isotope Reactor, a DOE Office of Science User Facility operated by the Oak Ridge National Laboratory. Work done at Ames National Laboratory (SLB and PCC) was supported by the U.S. Department of Energy, Office of Basic Energy Science, Division of Materials Sciences and Engineering. Ames National Laboratory is operated for the U.S. Department of Energy by Iowa State University under Contract No. DE-AC02-07CH11358. The experimental research at the University of Utah received support from the National Science Foundation Division of Materials Research Award No. 2132692. This work was also supported by the U.S. Department of Energy (DOE) Office of Science, Fusion Energy Sciences funding award entitled High Energy Density Quantum Matter, Award No DE-SC0020340. The experimental work took place at HPCAT (Sector 16, Advanced Photon Source, Argonne National Laboratory), which is supported by the DOE/National Nuclear Security Administration, Office of Experimental Sciences, with x-ray beam time and personnel support made possible by the Chicago/DOE Alliance Center, which is funded by the DOE/NNSA (DE-NA0003975). Instrumentation and facilities used were also supported by the National Science Foundation (DMR-1809783). The Advanced Photon Source is operated by the DOE Office of Sci-

ence by Argonne National Laboratory under Contract No. DE-AC02-06CH11357. The work of DP and LY at Oak Ridge National Laboratory (first principles calculations and interpretation) was supported by the U.S. Department of Energy, Office of Science, Basic Energy Sciences, Materials Science and Engineering Division. Measurements in pulsed magnetic fields were funded by DOE Basic Energy Sciences program “Science of 100 tesla.”

APPENDIX A: THE CRYSTAL STRUCTURE OF Y_2Co_3 UNDER HIGH PRESSURE

We investigated the pressure effects on the structural properties of Y_2Co_3 up to 19 GPa. High-pressure diffraction data were collected at the 16-BM-D beamline of the High Pressure Collaborative Access Team (HPCAT) at APS, ANL ($\lambda = 0.4133 \text{ \AA}$). Boehler-Almax plate diamond-anvil cells (DACs) with 350 or 500 μm culet size and a large opening angle of approximately 60° were utilized. The experiments involved high-pressure powder x-ray measurements conducted in two separate runs. All measurements were done at room temperature. Data collection between 3.65–9.8 GPa utilized silicon oil as the pressure-transmitting medium (PTM), while the second run, between 7.3–21 GPa, employed isopropanol as the PTM. We loaded the sample, along with ruby and gold, into a stainless steel gasket, which was then filled with the PTM. Pressure was determined using the ruby fluorescence method and the equation of state (EOS) of Au³⁴. The diffraction images were integrated using the Dioptas program³⁵. The powder XRD data were analyzed by the Le Bail fitting method using GSAS-EXPGUI package³⁶.

No structural phase transition was observed up to 21 GPa, and the sample remained in its ambient pressure $Cmce$ phase⁸. The sample exhibited a large bulk modulus of 80.7 GPa, which was determined with EoSFit7_GUI (Fig. 10)³⁷. The percentage of axial compression was similar along all axes but might be slightly higher along the b axis (Fig. 11). The b axis separates layers of Co and Y and controls the corresponding interlayer AFM coupling, which is expected to be strengthened under compression and help enhance the Néel temperature. Meanwhile, all primary intralayer FM couplings are weakened because of the compression along the $a - c$ planes. The overall changes in the magnetism of Y_2Co_3 , therefore, represent a balance of these two effects. Low-pressure data show that below 1 GPa, the Néel temperature decreases by a small amount of 1.6 K which is consistent with the similar compression rates of the sample along different axes.

APPENDIX B: THE SUBLATTICE MAGNETIC MOMENT AND PERPENDICULAR MAGNETIC SUSCEPTIBILITY

Following the molecular field theory, the sublattice magnetization at zero field can be calculated by solving the Brillouin function^{17,20,21}

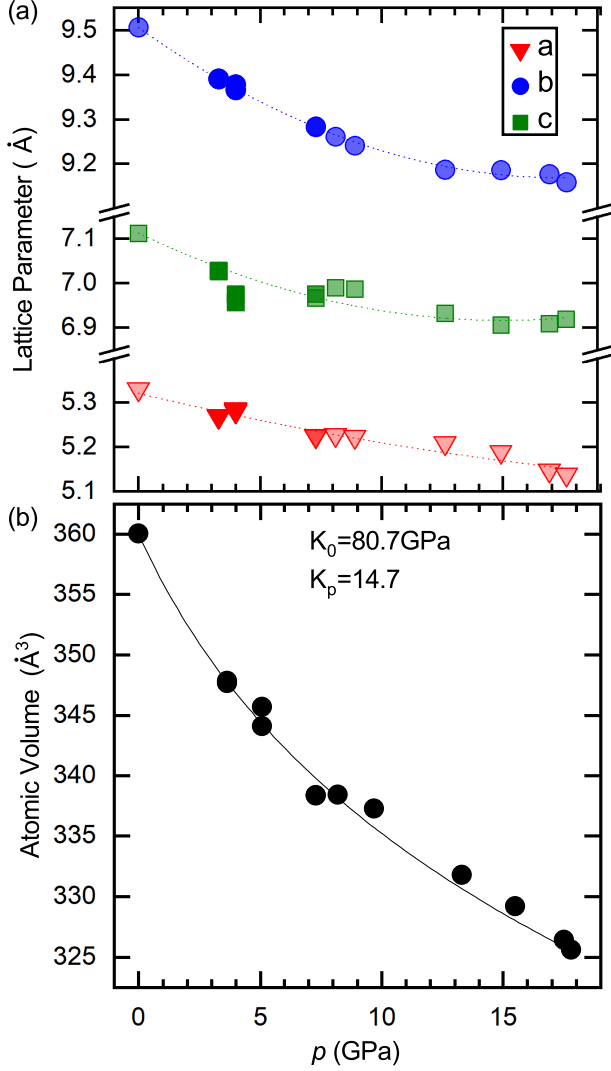


FIG. 10. (a) The lattice parameters a , b , c as a function of applied pressure. The dashed lines are polynomial fittings. (b) The unit-cell volume as a function of pressure. The solid line shows fourth-order Birch–Murnaghan fit to the experimental data.

$$M_1 = M_{sat} B_s \left(\frac{g\mu_B S}{k_B T} (\lambda_s M_1 + \lambda_d M_2) \right) \quad (6a)$$

$$M_2 = M_{sat} B_s \left(\frac{g\mu_B S}{k_B T} (\lambda_s M_2 + \lambda_d M_1) \right) \quad (6b)$$

In these equations, M_1 and M_2 are the magnetizations of two sublattices with opposite signs. $M_{sat} = \frac{1}{2} N g \mu_B S$ is the saturated magnetization of one sublattice. Under zero field, the magnitudes of the magnetization of two sublattices are the same. Thus, Eqs. (6a) and (6b) can be simplified as

$$\frac{M}{M_{sat}} = B_s \left(\frac{g\mu_B S}{k_B T} (\lambda_s - \lambda_d) M \right) \quad (7)$$

The temperature dependence of reduced sublattice magnetic moment can then be calculated with and without λ_d

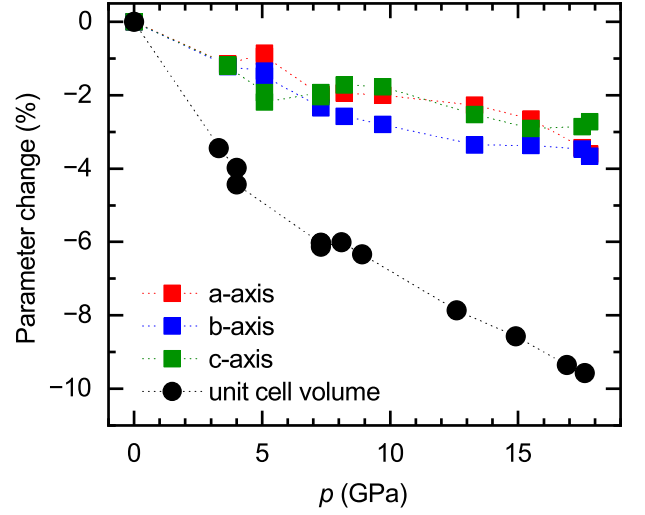


FIG. 11. Percentage change in lattice constants and unit-cell volume as a function of pressure.

changing with temperature. In the calculation, λ_s is a constant because the area of the ac plane almost remains temperature independent.

The comparison between the MFT calculation and the temperature-dependent ordered moment from neutron diffraction is shown in Fig. 12. The ordered moment is obtained from the square root of the Bragg peak intensity after the removal of the background signal above the transition temperature³⁸. Near the transition temperature, the MFT prediction with the temperature-dependent molecular field λ_d fits the experiment better. At low temperatures, both calculation curves can not describe the nonsaturation behavior, which is likely caused by the magnon excitation that is not discussed in the MFT model. A power law $C(1 - \frac{T}{T_N})^\beta$ is used to fit the ordered moment near the transition, which gives a β value of 0.34(2), relatively close to the critical exponent of the Heisenberg model, which is 0.367²¹.

As the magnetic field is applied perpendicular to the direction of the magnetic moments, the magnetization of each sublattice tilts slightly towards the direction of the magnetic field, producing a nonzero magnetic susceptibility. The tilted angle θ is determined by the competition between the AFM exchange energy, the Zeeman energy, and the magnetocrystalline anisotropy energy. The angle between the sublattice magnetization and the magnetic field is written as $\phi = 90^\circ - \theta$, and the angle between the two sublattices magnetization is 2ϕ .

The total energy of the two sublattices in a perpendicular magnetic field can be written as

$$E = -2MB \cos \phi + |\lambda_d| M^2 \cos 2\phi - K(1 - \cos^2 \phi) \quad (8)$$

In this equation, M is the magnetization of each sublattice. Taking $\frac{\partial E}{\partial \phi} = 0$, the energy is minimized when $\cos \phi = \frac{MB}{2|\lambda_d|M^2 + K}$. Thus, the total perpendicular magnetization is

$$M_\perp = 2M \cos \phi = \frac{2M^2 B}{2|\lambda_d|M^2 + K} \quad (9)$$

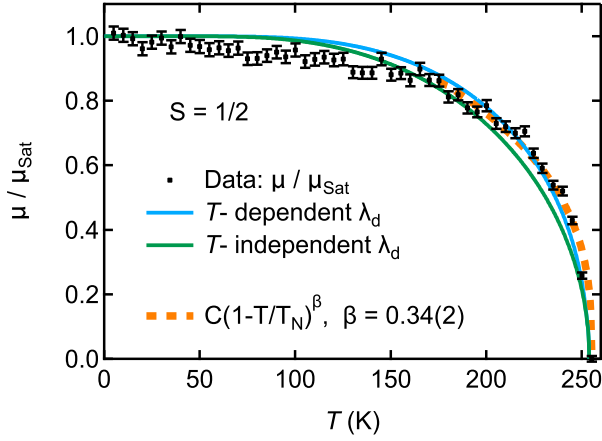


FIG. 12. The normalized ordered moment $\mu(T)/\mu_{sat}$ compared with the MFT calculations (solid lines) for spin $S = 1/2$. The orange-dash line is the fitting near the transition using the power law.

and the perpendicular magnetic susceptibility is

$$\chi_{\perp} = \frac{2M^2}{2|\lambda_d|M^2 + K} \quad (10)$$

As the magnetocrystalline anisotropy energy is much smaller than the exchange energy, Eq. (10) can be simplified as $\chi_{\perp} = \frac{1}{|\lambda_d|}$.

APPENDIX C: ESTIMATION OF CANTING ANGLE IN THE NON-COLLINEAR MODEL

We derive the canting angle based on a simple canting model shown in Fig. 13: a pair of spins are anti-aligned and canted from the b axis towards the c axis by an angle of α .

When an external magnetic field B is applied perpendicular to the magnetic moment, the susceptibility below T_N is independent of the temperature, $\chi = \chi(T_N)$. When the magnetic field is applied parallel to the direction of the magnetic moment, the magnetic susceptibility decreases from $\chi(T_N)$ to 0 as the temperature decreases²¹.

For a sample with a magnetic field applied along the b axis, the applied field has both parallel and perpendicular components relative to the moment direction. At low temperatures, the parallel component of the magnetic field yields zero magnetization, and the perpendicular magnetic field $B_{\perp} = B \sin \alpha$ would produce a magnetization

$$M(T = 0) = \chi(T_N)B_{\perp} = \chi(T_N)B \sin \alpha \quad (11)$$

Since our instrument measures the magnetization along the direction of the magnetic field, the measured b axis magnetization is

$$M_b(T = 0) = M(T = 0) \sin \alpha = \chi(T_N)B \sin^2 \alpha \quad (12)$$

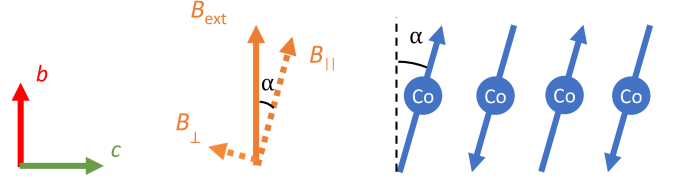


FIG. 13. An illustration of a simple canting model. The spins are anti-aligned and canted from the b axis toward the c axis by an angle of α . The external magnetic field is decomposed into a parallel and a perpendicular components relative to the direction of the magnetic moment.

Therefore, the measured susceptibility at zero temperature is

$$\chi_b(T = 0) = \frac{M_b(T = 0)}{B} = \chi(T_N) \sin^2 \alpha \quad (13)$$

$$\text{This yields } \sin^2 \alpha = \frac{\chi_b(T = 0)}{\chi(T_N)}.$$

APPENDIX D: THE SPIN-FLOP PHASE DIAGRAM AND TEMPERATURE DEPENDENCE OF MAGNETOCRYSTALLINE ANISOTROPY

Y_2Co_3 undergoes a spin-flop transition when the magnetic field is applied along the b axis at 21 T and 2 K⁸. In this study, we have taken a more comprehensive examination of the spin-flop transition phase diagram throughout the entire temperature range below T_N , as is shown in Fig. 15. We show a relatively good alignment between the experiment data and the theoretical calculation of the phase boundary based on a local moment collinear AFM model.

The high magnetic field measurements were performed using an extraction magnetometer in pulsed fields, with the sample immersed either in helium gas ($T > 4$ K) or ^4He liquid ($T < 4$ K). The extraction magnetometer enables measurements to be performed with and without the sample present to enable subtraction of the background⁴⁰.

The field dependence of magnetization $M(H)$ up to 60 T is shown in Fig. 14, without reaching saturation in both directions. Despite the relatively large effective moment of $2.5 \mu_B/\text{Co}$ derived from the Curie-Weiss fitting in the high-temperature paramagnetic regime, the field-dependent magnetization remains small, indicating that the AFM ordering is very robust. When the magnetic field is applied perpendicular to the easy axis [see Fig. 14(b)], an antiferromagnetic to paramagnetic transition occurs, which is more apparent in the derivative dM/dB curves in Fig. 14(c).

When the magnetic field is applied along the b axis, a spin-flop transition is observed at various temperatures [see Fig. 14(a)], in good agreement with previously reported results⁸. Such spin-flop transition corresponds to the reorientation of local moments from the b axis to the ac plane because of the competition between the Zeeman energy, exchange energy, and the magnetocrystalline anisotropy energy. In this

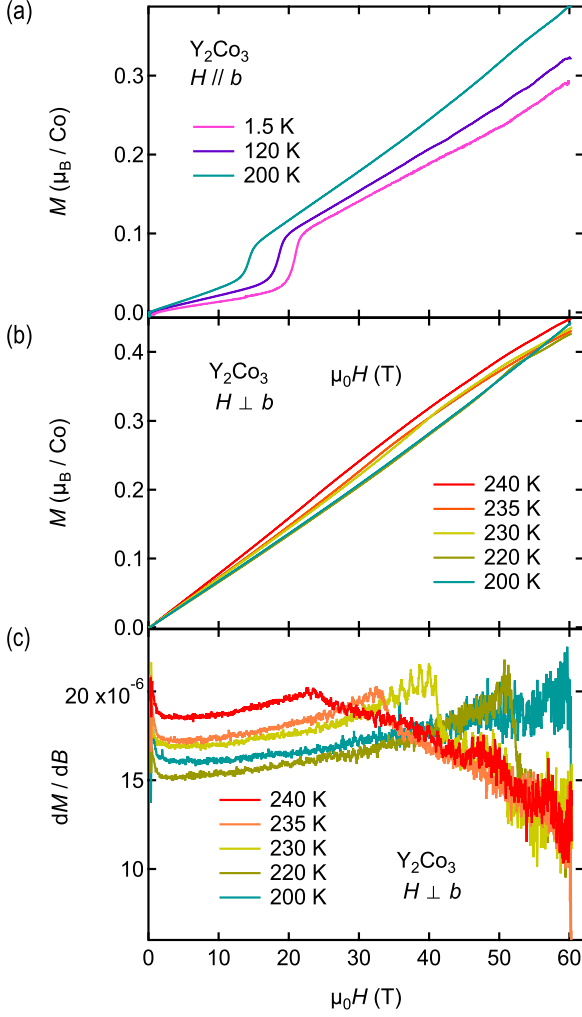


FIG. 14. (a) Magnetization as a function of applied magnetic field along the b axis and (b) in the ac plane. (c) Derivative of magnetization vs magnetic field.

paper, we simplify the magnetic structure to an A-type AFM structure and disregard the distinctions between the two cobalt sites. The temperature-dependent spin-flop field can be determined by the following equation⁸:

$$B_{SF}(T) = \sqrt{\frac{K(T)(2|\lambda_d|M^2 - K(T))}{M^2}} \quad (14)$$

Here, $K(T)$ is the temperature-dependent anisotropy energy, $|\lambda_d|M^2$ represents the exchange energy between two sublattices, and M is the sublattice magnetization per Co. We used $M_{sat}(T=0) = 1 \mu_B$ ($S = \frac{1}{2}$) in our simulation. At 2 K, $B_{SF}(0)$ and $K(0)$ were previously reported to be 21 T and 11.46 J per mol of pair of Co sites (or 5.73 J/mol-Co), respectively. The exchange energy term $|\lambda_d|M^2$ can also be determined to be 303 J per mol of Co. Converting this to $C\lambda_d$ at 2 K, we get -304 K, further confirming that the exchange energy is enhanced as the temperature decreases.

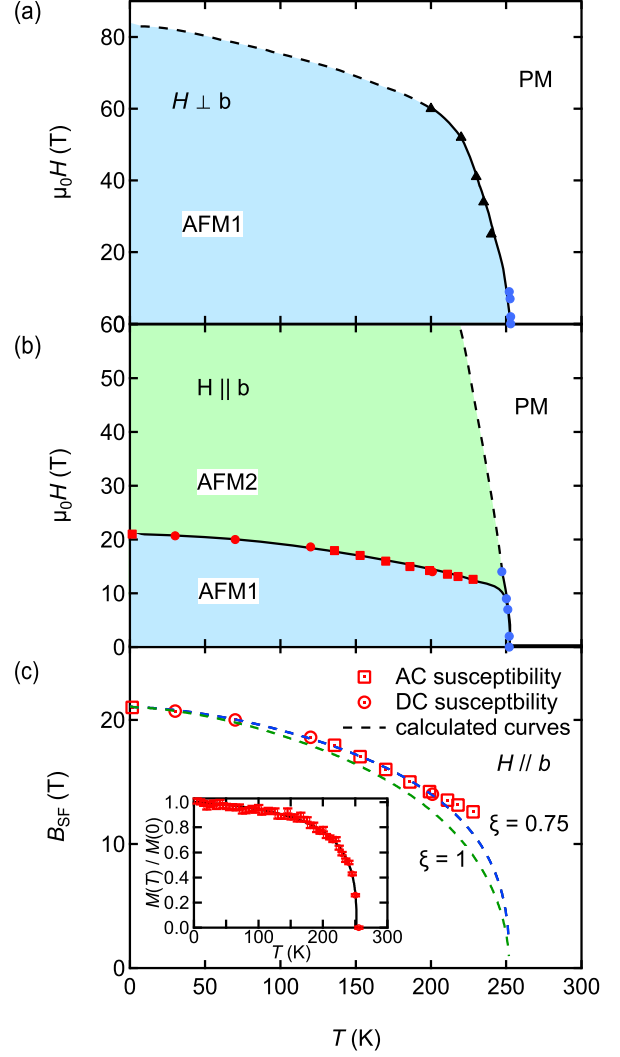


FIG. 15. (a) An illustration of the magnetic phase diagram with the magnetic field perpendicular to the b axis. The black triangle is from the DC pulse field result. The blue solid circle is from the resistivity measurement using PPMS. (b) The magnetic phase diagram with the magnetic field along the b axis. The blue region represents the original antiferromagnetic phase (AFM1), while the green region shows the spin-flop phase (AFM2). The red solid circle is from the DC pulse field result. The red solid square is from the AC susceptibility result⁸. The blue solid circle is from the resistivity measurement using PPMS. (c) The spin-flop phase diagram with B_{SF} as a function of temperature. The dashed line is the calculated curve of the phase boundary. The inset figure is the normalized magnetization of one sublattice below transition, obtained from the neutron magnetic Bragg peak intensity. The solid line is the fitting curve using the Kuz'min equation³⁹.

The temperature dependence of $K(T)$ is given by the Callen-and-Callen (CC) law⁴¹⁻⁴³. In a uniaxial system, the temperature-dependent anisotropy can be written as

$$K_1(T) = (K_1^0 + \frac{7}{8}K_2^0) \left(\frac{M(T)}{M(0)}\right)^3 - \frac{7}{8}K_2^0 \left(\frac{M(T)}{M(0)}\right)^{10} \quad (15)$$

$$K_2(T) = K_2^0 \left(\frac{M(T)}{M(0)}\right)^{10} \quad (16)$$

Considering that the K_2 term is usually negligible, the equation can be reduced to

$$K(T) = K_0 \left(\frac{M(T)}{M(0)}\right)^3 \quad (17)$$

In an antiferromagnet, however, it is not rigorous to directly apply this power law by taking $M(T)$ as the sublattice magnetization. Equation (17) is modified as⁴⁴

$$K(T) = K_0 \left(\frac{M(T)}{M(0)}\right)^{3\xi} \quad (18)$$

Note that the equation above is obtained based on a particular model with a single-ion mechanism spin-wave calculation, and is not accurate in a complicated magnetic system such as Y_2Co_3 . Thus, this is only a rough representation of the experimental data. In this paper, the $\frac{M(T)}{M(0)}$ of Y_2Co_3 is determined by the Bragg peak intensity of single-crystal neutron scattering, as mentioned in Appendix B. The curve is fitted using the so-called Kuz'min equation, as shown in Fig. 15(a),

$$m(\tau) = [1 - s\tau^{3/2} - (1-s)\tau^p]^{1/3} \quad (19)$$

In this equation, $m = M_s/M_0$ is the normalized spontaneous magnetization, $\tau = T/T_C$ (or T/T_N in AFM). s and p are the parameters that determine the shape of the magnetization curve, and are fitted to be 0.63 and 5.4, respectively. The temperature dependence of anisotropy $K(T)$ and spin-flop field B_{SF} can then be represented as

$$K(T) = K_0[1 - s\tau^{3/2} - (1-s)\tau^p]^\xi \quad (20)$$

and

$$B_{SF}(T) = \{2|\lambda_d|K_0[1 - s\tau^{3/2} - (1-s)\tau^p]^\xi - \frac{K_0^2}{M_s^2}[1 - s\tau^{3/2} - (1-s)\tau^p]^{4/3\xi}\}^{1/2} \quad (21)$$

The calculated spin-flop field as a function of temperature is shown in Fig. 15(b) and compared with the experiment data of AC susceptibility measurement (circle) and DC pulse measurement (square). The calculated phase boundary with $\xi = 0.75$ is in better agreement with the experiment result below 200 K compared to $\xi = 1$. Above 200 K the spin-flop transition becomes very broad owing to the thermal fluctuation near the transition temperature, which may cause the deviation between the experiment data and the calculated curve.

* vtaufour@ucdavis.edu

¹ T.-H. Han, J. S. Helton, S. Chu, D. G. Nocera, J. A. Rodriguez-Rivera, C. Broholm, and Y. S. Lee, *Nature* **492**, 406 (2012).
² B. C. Sales, W. R. Meier, A. F. May, J. Xing, J.-Q. Yan, S. Gao, Y. H. Liu, M. B. Stone, A. D. Christianson, Q. Zhang, and M. A. McGuire, *Phys. Rev. Mater.* **5**, 044202 (2021).
³ S. Nakatsuji, N. Kiyohara, and T. Higo, *Nature* **527**, 212 (2015).
⁴ W. Ma, X. Xu, Z. Wang, H. Zhou, M. Marshall, Z. Qu, W. Xie, and S. Jia, *Physical Review B* **103**, 1 (2021).
⁵ T. Mahon, E. Gaudin, B. Vignolle, G. Ballon, B. Chevalier, and S. Tencé, *Journal of Alloys and Compounds* **737**, 377 (2018).
⁶ S. Tencé, R. Caballero Flores, J. Chable, S. Gorsse, B. Chevalier, and E. Gaudin, *Inorganic Chemistry* **53**, 6728 (2014).
⁷ J. K. Byland, Y. Shi, D. S. Parker, J. Zhao, S. Ding, R. Mata, H. E. Magliari, A. Palasyuk, S. L. Bud'ko, P. C. Canfield, P. Klavins, and V. Taufour, *Phys. Rev. Materials* **6**, 063803 (2022).
⁸ Y. Shi, D. S. Parker, E. S. Choi, K. P. Devlin, L. Yin, J. Zhao, P. Klavins, S. M. Kauzlarich, and V. Taufour, *Phys. Rev. B* **104**, 184407 (2021).
⁹ D. Gignoux, R. Lemaire, R. Mendia-Monterroso, J. Moreau, and J. Schweizer, *Physica B+ C* **130**, 376 (1985).
¹⁰ M. Brouha and K. H. J. Buschow, *Journal of Physics F: Metal Physics* **3**, 2218 (1973).
¹¹ A. Jesche and P. C. Canfield, *Philosophical Magazine* **94**, 2372 (2014).
¹² H. Cao, B. C. Chakoumakos, K. M. Andrews, Y. Wu, R. A. Riedel,

J. Hodges, W. Zhou, R. Gregory, B. Haberl, J. Molaison, and G. W. Lynn, *Crystals* **9** (2019), 10.3390/cryst9010005.
¹³ B. C. Chakoumakos, H. Cao, F. Ye, A. D. Stoica, M. Popovici, M. Sundaram, W. Zhou, J. S. Hicks, G. W. Lynn, and R. A. Riedel, *Journal of Applied Crystallography* **44**, 655 (2011).
¹⁴ J. Perez-Mato, S. Gallego, E. Tasci, L. Elcoro, G. de la Flor, and M. Aroyo, *Annual Review of Materials Research* **45**, 217 (2015).
¹⁵ J. Rodríguez-Carvajal, *Physica B: Condensed Matter* **192**, 55 (1993).
¹⁶ K. Nawa, D. Okuyama, H.-C. Wu, R. Murasaki, S. Matsuzaka, K. Kinjo, and T. J. Sato, *Journal of the Physical Society of Japan* **93**, 091001 (2024), <https://doi.org/10.7566/JPSJ.93.091001>.
¹⁷ D. C. Johnston, *Phys. Rev. Lett.* **109**, 077201 (2012).
¹⁸ I. Živković, K. Prša, O. Zaharko, and H. Berger, *Journal of Physics: Condensed Matter* **22**, 56002 (2010).
¹⁹ E. D. Mun, S. L. Bud'ko, H. Ko, G. J. Miller, and P. C. Canfield, *Journal of Magnetism and Magnetic Materials* **322**, 3527 (2010).
²⁰ D. C. Johnston, R. J. McQueeney, B. Lake, A. Honecker, M. E. Zhitomirsky, R. Nath, Y. Furukawa, V. P. Antropov, and Y. Singh, *Phys. Rev. B* **84**, 094445 (2011).
²¹ S. J. Blundell, *Magnetism in Condensed-Matter* (Oxford University Press, Oxford, 2001).
²² C. Kittel, *Introduction to Solid State Physics*, 8th ed. (Wiley, Hoboken, NJ, 2004).
²³ T. Tsuda, H. Yasuoka, and T. Miyauchi, *Journal of the Physical Society of Japan* **45**, 1551 (1978),

- <https://doi.org/10.1143/JPSJ.45.1551>.
- ²⁴ D. Breed, K. Gilijamse, and A. Miedema, *Physica* **45**, 205 (1969).
- ²⁵ Y. S. Tang, S. M. Wang, L. Lin, C. Li, S. H. Zheng, C. F. Li, J. H. Zhang, Z. B. Yan, X. P. Jiang, and J.-M. Liu, *Phys. Rev. B* **100**, 134112 (2019).
- ²⁶ S. McAlister and P. Strobel, *Journal of Magnetism and Magnetic Materials* **30**, 340 (1983).
- ²⁷ F. Hardy, C. Meingast, V. Taufour, J. Flouquet, H. v. Loehneysen, R. A. Fisher, N. E. Phillips, A. D. Huxley, and J. C. Lashley, *Phys. Rev. B* **80**, 174521 (2009).
- ²⁸ K. N. Shrivastava, *phys. stat. sol. (b)* **78**, 749 (1976), <https://onlinelibrary.wiley.com/doi/pdf/10.1002/pssb.2220780236>.
- ²⁹ M. E. Fisher, *Journal of Mathematical Physics* **4**, 124 (1963).
- ³⁰ E. Svanidze, J. K. Wang, T. Besara, L. Liu, Q. Huang, T. Siegrist, B. Frandsen, J. W. Lynn, A. H. Nevidomskyy, M. B. Gamza, M. C. Aronson, Y. J. Uemura, and E. Morosan, *Nature Communications* **6** (2015), 10.1038/ncomms8701.
- ³¹ R. E. Baumbach, V. A. Sidorov, X. Lu, N. J. Ghimire, F. Ronning, B. L. Scott, D. J. Williams, E. D. Bauer, and J. D. Thompson, *Phys. Rev. B* **89**, 094408 (2014).
- ³² M. Rotter, M. Tegel, D. Johrendt, I. Schellenberg, W. Hermes, and R. Pöttgen, *Phys. Rev. B* **78**, 020503(R) (2008).
- ³³ D. Paige, B. Szpunar, and B. Tanner, *Journal of magnetism and magnetic materials* **44**, 239 (1984).
- ³⁴ O. L. Anderson, D. G. Isaak, and S. Yamamoto, *Journal of Applied Physics* **65**, 1534 (1989).
- ³⁵ C. Prescher and V. B. Prakapenka, *High Pressure Research* **35**, 223 (2015), <https://doi.org/10.1080/08957959.2015.1059835>.
- ³⁶ C. H. Lake and B. H. Toby, *Powder Diffraction* **26**, S13–S21 (2011).
- ³⁷ G. Shen, Y. Wang, A. Dewaele, C. Wu, D. E. Fratanduono, J. Eggert, S. Klotz, K. F. Dziubek, P. Loubeyre, O. V. Fat'yanov, P. D. Asimow, T. Mashimo, and R. M. M. Wentzcovitch, *High Pressure Research* **40**, 299 (2020), <https://doi.org/10.1080/08957959.2020.1791107>.
- ³⁸ S. Pakhira, F. Islam, E. O'Leary, M. A. Tanatar, T. Heitmann, L.-L. Wang, R. Prozorov, A. Kaminski, D. Vaknin, and D. C. Johnston, *Phys. Rev. B* **106**, 024418 (2022).
- ³⁹ M. D. Kuz'min, *Phys. Rev. Lett.* **94**, 107204 (2005).
- ⁴⁰ J. A. Detwiler, G. M. Schmiedeshoff, N. Harrison, A. H. Lacerda, J. C. Cooley, and J. L. Smith, *Phys. Rev. B* **61**, 402 (2000).
- ⁴¹ E. Callen and H. Callen, *Journal of Physics and Chemistry of Solids* **16**, 310 (1961).
- ⁴² E. R. Callen, *Journal of Applied Physics* **33**, 832 (2004).
- ⁴³ T. N. Lamichhane, O. Palasyuk, V. P. Antropov, I. A. Zhuravlev, K. D. Belashchenko, I. C. Nlebedim, K. W. Dennis, A. Jesche, M. J. Kramer, S. L. Bud'ko, R. W. McCallum, P. C. Canfield, and V. Taufour, *Journal of Magnetism and Magnetic Materials* **513**, 167214 (2020).
- ⁴⁴ H. Callen and E. Callen, *Journal of Physics and Chemistry of Solids* **27**, 1271 (1961).